Journal of Materials Chemistry A

Computational Discovery of Diverse Functionalities in Two-Dimensional Square Disulfide Monolayers: Auxetic Behavior, High Curie Temperature Ferromagnets, Electrocatalysts, and Photocatalysts

Journal:	*Journal of Materials Chemistry A*
Manuscript ID	TA-ART-06-2023-003699.R1
Article Type:	Paper
Date Submitted by the Author:	18-Aug-2023
Complete List of Authors:	Liu, Yu; Inner Mongolia University, School of Physical Science and Technology Li, Wenlong ; Inner Mongolia University Li, Fengyu; Inner Mongolia University, School of Physical Science and Technology Chen, Zhongfang; University of Puerto Rico, Chemistry

Computational Discovery of Diverse Functionalities in Two-Dimensional Square Disulfide Monolayers: Auxetic Behavior, High Curie Temperature Ferromagnets, Electrocatalysts, and Photocatalysts

Yu Liu[1], Wenlong Li[1], Fengyu Li[1,*], Zhongfang Chen[2,*]

[1] *School of Physical Science and Technology, Inner Mongolia University, Hohhot, 010021, China*
[2] *Department of Chemistry, The Institute for Functional Nanomaterials, University of Puerto Rico, Rio Piedras Campus, San Juan, PR 00931, USA*
* Corresponding Authors: fengyuli@imu.edu.cn (FL); zhongfang.chen1@upr.edu (ZC)

Abstract:

By means of systematic density functional theory (DFT) computations, we identified 12 stable two-dimensional (2D) disulfide monolayers featuring a square lattice from a pool of 68 candidate monolayers. Our screening process comprehensively assessed their thermodynamic, dynamic, mechanical, and thermal stabilities. These 12 stable monolayers (S-XS2 with X = Si, Ge, Sn, Pb, Ti, V, Cr, Mn, Zr, Mo, Re, and Os) all exhibit low in-plane Young's moduli (25.30~96.09 Nm−1). Notably, four *S*-XS_2 (X = Si, Ge, Sn, and Pb) monolayers possess negative Poisson's ratios (NPRs). The magnetic and electronic properties vary across the monolayers, with *S*-ReS_2 and *S*-OsS_2 being nonmagnetic and metallic, *S*-MoS_2 being antiferromagnetic and metallic, and *S*-SiS_2, *S*-GeS_2, *S*-SnS_2, *S*-PbS_2, *S*-ZrS_2, and *S*-TiS_2 being nonmagnetic and semiconducting (bandgaps ranged in 1.59~2.79 eV). The *S*-VS_2 monolayer exhibits ferromagnetic half-semiconductor behavior, while *S*-CrS_2 and *S*-MnS_2 are ferromagnetic half-metals. The carrier mobilities of the seven semiconducting monolayers range widely (0.20~17068.47 $cm^2V^{-1}s^{-1}$), and hole mobility could be controlled through uniaxial strains in *S*-ZrS_2, *S*-TiS_2, and *S*-VS_2. Additionally, certain monolayers (*S*-XS_2 with X = V, Cr, and Mn) have high Curie temperatures and magnetic anisotropy energies. Two semiconducting monolayers (*S*-XS_2 with X = Si and Ge) are promising candidates for photocatalyzing water splitting, and the metallic or half-metallic *S*-ReS_2 and *S*-OsS_2 can boost electrochemical hydrogen evolution reaction. This work not only adds novel members to the family of 2D materials, but also provides theoretical guidance for further explorations to both experimental and theoretical communities.

1. Introduction

Since the experimental realization of graphene in 2004,[1] graphene and other two-dimensional (2D) materials have become a focal point of cutting-edge research. Significant progress has been made both experimentally and theoretically.[2–6] One particularly exciting area of research involves the investigation of 2D transition metal compounds (TMCs) due to their diverse and intriguing physical properties, including electrical, mechanical, and optical characteristics.[7–11] Notably, certain TMCs have demonstrated potential as electrocatalysts for hydrogen evolution reactions and as photocatalysts for water splitting, making them promising candidates for clean energy solutions and environmental purification processes.[12–15] The pursuit of materials with auxetic properties, characterized by a negative Poisson's ratio (NPR) and counterintuitive behavior, has been an active area of research. Three groups of 2D NPR materials have been identified so far: (i) in-plane NPR materials (eg. silicon dioxide,[16] and pentagraphene),[17] out-plane NPR materials (eg. borophane,[18] and black phosphorus),[19] and three-dimensional (3D) NPR materials (eg. $GaPS_4$,[20] and *S*-SN_2 monolayers).[21] TMC materials, such as 1T-type MX_2 (M = Mo, W, Tc, Re; X = S, Se, Te) and MXene W_2C monolayers with in-plane NPR behavior,[22,23] and Ag_2S monolayers with 3D NPR behavior,[24] further expand the scope of these exceptional materials and their potential applications in various fields.

Furthermore, 2D TMCs possess a diverse range of electronic properties, including semiconducting, metallic, and superconducting behaviors. This versatility enables their application in various fields, such as electrode materials for lithium-ion batteries, [25]

electronic/optoelectronic devices,[26,27] and superconductors.[28] Importantly, TMC materials can serve as electrocatalysts for the hydrogen evolution reaction (HER) and photocatalysts for water splitting, addressing the challenges of the energy crisis and environmental pollution by offering potential solutions for clean energy generation and environmental purification.

Despite the progress made, challenges persist in both electrocatalytic and photocatalytic applications. Metallic materials with good conductivity are a prerequisite for HER electrocatalysts.[29,30] Current electrocatalysts for HER, primarily Pt-based nanomaterials, face limitations due to their high cost and poor stability. [31] Typically, semiconductors with appropriate bandgaps are required for water-splitting photocatalysts, as they can generate electron-hole pairs, thereby initiating the necessary redox reactions for hydrogen generation.[32,33] Unfortunately, most photocatalysts suffer from drawbacks such as large band gaps, low utilization of visible light, and fast recombination rates of photo-generated carriers.[34] Thus, there is a fundamental need to design suitable metallic electrocatalysts and semiconducting photocatalysts to advance green hydrogen production.

2D TMCs have emerged as promising alternatives to Pt-based catalysts due to their unique advantages, including large specific surface area, mechanical stability, tunable electrical properties, [35] and composition of earth-abundant elements. Various 2D TMCs, such as transition metal chalcogenides, phosphides, carbides, and borides,[36-39] have been studied as electrocatalysts for HER. For instance, MoS_2, a representative 2D TMC, has shown promising HER activity, particularly in the metastable 1T phase,[40] and the

S edge sites in the 2H-MoS_2 phase.[41,42] However, achieving the desired catalytic performance for hydrogen evolution remains a challenge, necessitating the exploration of other 2D TMCs, including new phases.

In the field of photocatalytic water splitting, extensive research has been conducted on various photocatalysts, such as metal sulfides,[43] metal-organic frameworks (MOFs),[44] graphitic carbon nitride (g-C_3N_4),[45] and metal oxides.[46] TiO_2, the first photocatalyst used in water splitting and widely industrialized,[47] still faces limitations due to its wide band gap, restricting its absorption to ultraviolet (UV) light. Metal sulfides have garnered attention as potential alternatives due to their narrower band gaps and superior light absorption properties, enabling enhanced utilization of solar energy.[48] However, challenges, such as photocorrosion, low density of active sites, and rapid recombination of excited electrons and holes,[49] impede the efficiency and stability of metal sulfide photocatalysts. Overcoming these limitations is crucial to unlock the full potential of metal sulfides as efficient and robust photocatalysts for water splitting.

In short, there is an urgent need to design and search for stable semiconducting or metallic materials with exceptional properties for various important applications. Considering that 2D transition metal dichalcogenides (TMDs) have rich content, adjustable band gap, high mechanical strength, considerable optical absorption, and other excellent properties,[50–53] in this work, we will focus on exploring 2D TMDs that go beyond the extensively studied hexagonal structures. Specifically, we will investigate 2D TMDs with a square lattice structure, which presents a unique

opportunity to uncover novel properties and potential applications in this distinct class of materials.

The 2D TMDs with square lattice have emerged as a new type of 2D materials. Theoretically, Gu *et al*. predicted a series of such materials, which are promising either as the catalysts for HER or anodes for lithium-ion batteries,[54] Qiao *et al.* found that the SeN_2 monolayer is the only stable 2D crystal among 11 V-VI binary nanosheets with square lattice.[55] Experimentally, by Au-assisted mechanical exfoliation, Huang *et al.* prepared more than 40 types of large-area single-crystalline monolayers, among which is GeS_2 in *P*-4*m*2 symmetry with square lattice, but its properties have not been studied so far.[56]

The above exciting findings, especially the successful synthesis of the square configuration of the GeS_2 monolayer, prompt important questions: Would the other 2D TMDs adopt a square structure? Can other main group elements form a stable 2D square lattice? What are the properties and applications associated with these square monolayers? To address these queries, we systematically constructed 68 square disulfide monolayers by combining sulfur with elements across the periodic table (Fig. 1). By examining the thermodynamical, dynamical, mechanical, and thermal stabilities using first-principles calculations, 12 square structures were verified to be stable, namely, *S*-XS_2 (X = Si, Ge, Sn, Pb, Ti, V, Cr, Mn, Zr, Mo, Re, and Os). These 12 *S*-XS_2 monolayers exhibit diverse mechanical, magnetic, and electronic properties, making them potential candidates as photocatalysts for water splitting or electrocatalysts for hydrogen evolution reactions (HER). Thus, our theoretical

investigations provide valuable guidance for further exploration of 2D disulfides, both theoretically and experimentally.

2. Computational methods

First-principles calculations were performed using the Vienna *ab initio* simulation package (VASP)[57] with the plane-wave basis set and the projector augmented wave (PAW) method.[58,59] The exchange-correlation interactions were described by the Perdew, Burke and Ernzerhof (PBE) functional within the generalized gradient approximation (GGA).[60] A 500 eV energy cuttoff was used, and to account for 2D materials, a vacuum of more than than 15 Å was included to avoid spurious interactions between periodic images. All atomic positions and lattice constants were relaxed using the conjugate gradient method. Convergence criteria of 10^{-5} eV for the total energy and 0.01 eV $Å^{-1}$ for the residual force on each atom were applied.

For the 2D *S*-XS_2 systems (Fig. 1a), the Brillouin zone of the unit cell (Fig. 1b) was sampled using the Monkhorst-Pack (MP) scheme[61] of an 11×11×1 *k*-point grid. Hirshfeld charge analysis was conducted by DMol^3 code. To address the underestimation of band gaps by the standard GGA functional, we utilized the hybrid functional (HSE06)[62] to better predict the band structures of *S*-XS_2 monolayer system. Spin–orbit coupling (SOC) was included when calculating the magnetic anisotropy energy (MAE), which was obtained as the energy difference between magnetization directions in the *xy* plane ($E\parallel$) and along the *z* axis ($E\perp$), where MAE = $E\parallel - E\perp$. For E$\parallel$, magnetization directions along both (100) and (101) were considered, while E$\perp$

represented the energy for the (001) magnetization. Positive and negative MAE values indicate the easy magnetization axis along the out-of-plane and in-plane directions, respectively.

To assess the stability of the *S*-XS_2 monolayers, various computational methods were employed. Cohesive energy calculations were conducted to examine the thermodynamic stability. The dynamic stability was evaluated through phonon dispersion calculations using the Phonopy code, which is based on density functional perturbation theory (DFPT) implemented in VASP. [63] Elastic constants were used to examine the mechanical stability. The thermal stability was investigated by first-principles molecular dynamics (FPMD) simulations with the PAW method and the PBE functional. In the FPMD simulations, an initial configuration of the *S*-XS_2 system, consisting of a 6×6×1 supercell with 108 atoms, was annealed at room temperature (300 K). Each FPMD simulation in an NVT canonical ensemble was performed for a duration of 5 ps with a time step of 1 fs.

3. Results and discussion

3.1 Geometric structures of the *S*-XS_2 monolayers

Based on the reported GeS_2 monolayer with the symmetry of *P*-4*m*2,[56] we constructed 68 two-dimensional (2D) disulfides with a square lattice (denoted as *S*-XS_2), by substituting Ge with other elements in the periodic table. These elements include 39 main group elements (H~Po excluding S) and 29 transition metal elements (Sc~Hg). Fig. 1a illustrates the primitive cell of the *S*-XS_2 monolayer, consisting of one X and two S atoms. Each X atom is tetra-coordinated with four S atoms, and each S atom

bridges two X atoms, thus forming a triple-layer structure. Key geometric parameters of the optimized *S*-XS_2 monolayers, including the lattice constant (a), monolayer thickness (h), bond lengths (r_{X-S}), and bond angle (θ) are presented in Table S1.

Note that out of the 68 monolayers, ten (*S*-PS_2, *S*-OS_2, *S*-FS_2, *S*-HeS_2, *S*-NeS_2, *S*-ArS_2, *S*-KrS_2, *S*-XeS_2, *S*-ZnS_2, and *S*-HgS_2) exhibit significant distortion of the square lattice or lack of bonding between S and X atoms, indicating that the 2D square configuration is not favored for these species. Thus, we will focus on the remaining 58 monolayers whose optimized structures maintain the original symmetry. Generally, the lattice constants, monolayer thickness, and bond lengths of these *S*-XS_2 monolayers are well correlated with the radius of X. For example, the a, h, and r_{X-S} values increase from 2.81, 3.07, and 2.08 Å for Be to 4.13, 4.19 and 2.94 Å for Ba, respectively.

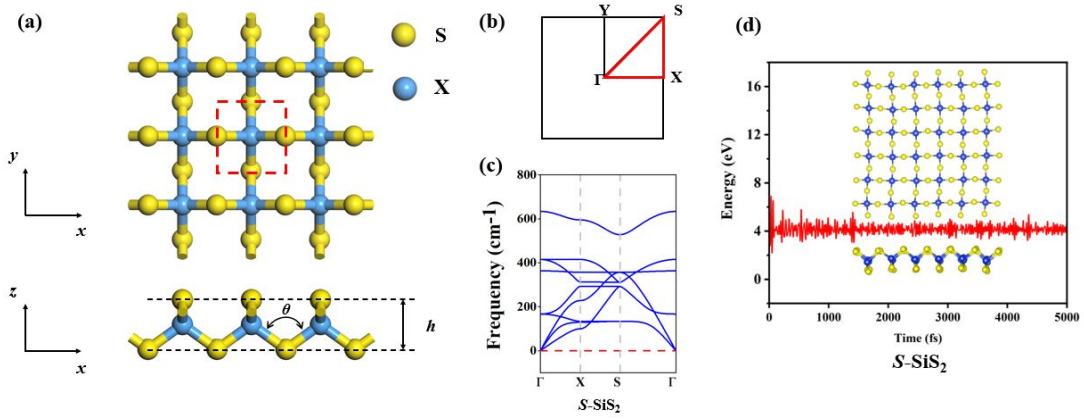

Fig. 1 (a) Top and side views of the 3×3×1 supercell of *S*-XS_2 monolayer (the primitive cell is marked by red rectangle dash lines; the yellow and blue balls represent S and X atoms, respectively). (b) The first Brillouin zone (BZ) of *S*-XS_2 monolayers with high symmetric k points. (c) The phonon dispersion of *S*-SiS_2. (d) The final structure and energy fluctuation of *S*-SiS_2 that have undergone 5 ps FPMD simulations at 300 K.

3.2 Evaluation of Stabilities

After relaxation, the 58 *S*-XS_2 candidates remain the same symmetry as GeS_2 reported in Ref. 56. To assess their potential for experimental realization, we systematically examined their thermodynamic, dynamic, mechanical, and thermal stabilities.

First, we calculated the cohesive energy (E_{coh}) of *S*-XS_2 structures to evaluate their thermodynamic stability, which is defined as:

$$E_{coh} = (nE_X + mE_S - E_{tot})/(n + m) \quad \text{(Equation 1)}$$

where E_{tot} is the total energy of the monolayer, E_X/E_S is the energy of an isolated X/S atom, and n/m is the number of X/S atoms in the system. According to this definition, a more positive E_{coh} indicates greater thermodynamic stability. The calculated cohesive energies of the 58 *S*-XS_2 structures (ranging from 0.61 to 5.52 eV/atom) are comparable to or higher than those of the corresponding hexagonal structures (1.52~5.91 eV/atom, Table S1). In addition, after relaxation, some hexagonal structures, such as BS_2, even transformed to their square counterparts. Notably, the E_{coh} values of 34 *S*-XS_2 monolayers (E_{coh} > 3.00 eV/atom) are also comparable to that of silicene (3.98 eV/atom) and germanene (3.26 eV/atom),[64] implying a high likelihood of their synthesis in the laboratory using the widely employed chemical vapor deposition method for metal chalcogenides.[65,66]

Then, the dynamic stability of the *S*-XS_2 monolayers was investigated by calculating their phonon dispersions. Out of the 58 monolayers, 37 *S*-XS_2 structures (X = Be, B, Al, Ga, In, Tl, Si, Ge, Sn, Pb, As, Sb, Bi, Ti, V, Cr, Mn, Fe, Co, Ni, Cu, Zr, Nb, Mo, Tc, Ru, Rh, Ag, Cd, Hf, Ta, W, Re, Os, Ir, Pt, and Au) are dynamically stable as

demonstrated by the all positive frequencies or very small imaginary frequencies throughout the entire BZ (the phonon dispersion of *S*-SiS_2 is given in Fig. 1c as a representative, see Fig. S1 for details). The *S*-InS_2 and *S*-CuS_2 monolayers have tiny U-shape negative frequencies (−5 and −5 cm^{-1}, respectively) near the Γ point, which have been observed in various 2D materials[67] and do not compromise their dynamic stability. Conversely, the remaining 21 structures have large negative frequencies (Fig. S2) and deemed dynamically unstable. Particularly, the highest frequencies of the dynamically stable *S*-XS_2 monolayers (212~760 cm^{-1}) surpass or match those of hexagonal MoS_2 monolayer (473 cm^{-1}),[68] and black phosphorene (440 cm^{-1}),[69] underscoring the strong chemical bonding in these 2D *S*-XS_2 crystals.

We further assessed the mechanical stability of the 37 thermodynamically and dynamically stable *S*-XS_2 monolayers. Table S2 summarizes their elastic constants (C_{11}, C_{22}, C_{12} and C_{66}), Young's moduli (Y), and Poisson's ratios (ν). According to the Born criteria for 2D materials ($C_{11}C_{22} - C_{12}^2 > 0$ and $C_{66} > 0$),[70] 27 *S*-XS_2 monolayers (X = B, Al, Ga, In, Tl, Si, Ge, Sn, Pb, Ti, V, Cr, Mn, Fe, Co, Zr, Nb, Mo, Ru, Rh, Ag, Hf, Ta, W, Re, Os, and Ir) are mechanically stable. Interestingly, seven *S*-XS_2 monolayers (X = Si, Ge, Sn, Pb, Fe, Rh, and Ag) display a negative Poisson's ratio (NPR), as indicated in Table S2. Detail discussions on the mechanical properties are given in the section addressing mechanical properties.

We performed first-principles molecular dynamics (FPMD) simulations to examine the thermal stability of the screened 27 *S*-XS_2 monolayers. A 6×6×1 supercell was used, and the monolayers were heated at room temperature (300 K) for 5 ps with a time step

of 1 fs. The total energies of 12 *S*-XS_2 monolayers (X = Si, Ge, Sn, Pb, Ti, V, Cr, Mn, Zr, Mo, Re, and Os) fluctuated with the amplitudes comparable to those of the experimentally synthesized *S*-GeS_2 sheet. Notably, all these 12 structures were well preserved throughout 5 ps FPMD simulations (the final structure and energy fluctuation of *S*-SiS_2 are given in Fig. 1d as a representative, see Fig. S3 for details). In contrast, the remaining 15 structures were seriously distorted (Fig. S4), indicating a lack of thermal stability in those cases. Thus, our simulations indicate that the 12 *S*-XS_2 structures have good thermal stability.

In short, the above stability evaluations demonstrate that the 12 *S*-XS_2 monolayers exhibit great stabilities in thermodynamic, dynamic, mechanic, and thermal aspects, including four main-group based (X = Si, Ge, Sn, and Pb) and eight transition metal-based sheets (X = Ti, V, Cr, Mn, Zr, Mo, Re, and Os).

In addition to the above stability evaluations, we also performed a global minimum search for 2D SiS_2 using the CALYPSO code,[71] which identified the S-SiS_2 monolayer as the lowest-energy structure. The other two low-lying structures, namely, SiS_2-2 and SiS_2-3, have rather close cohesive energies (Table S3), are both mechanically and dynamically stable (Table S2 and Fig. S5), and are indirect bandgap semiconductors. In addition, recently studies confirmed that *S*-PbS_2 is the most stable structure globally using the CALYPSO method.[72] Though the remaing 10 *S*-XS_2 monolayers have not been confirmed as the global minima, their exceptional stabilities make them highly promising for experimental realization.

To gain insights into the stability of the 12 stable *S*-XS_2 monolayers in terms of chemical bonding, we calculated their electron localization functions (ELF).[73] Generally, the ELF values provide information about electron localization, with values of 1.0 indicating complete localization and 0.5 representing a free electron gas. Areas of low electron density are indicated by ELF values close to zero.

As displayed in Fig. S6, the four *S*-XS_2 (X = Si, Ge, Sn, Pb) structures exhibit covalent bonding, as a significant number of electrons are accumulated between S and X atoms. In contrast, the other eight *S*-XS_2 monolayers have distinct bonding characteristics, where the electrons are mainly localized around S atoms with relatively fewer electrons around the X atoms, indicating the coexistence of ionic and covalent bonding, with tightly bonded atoms and electron transfers from the X atoms to S atoms. This observation is further supported by Bader charge analysis (each X atom donates 0.61~2.31 electrons to the adjacent S atoms) and Hirschfeld charge analysis (electron transfer of 0.02~0.46 electrons) (Table S4).

3.3 The mechanical properties

We then examined the mechanical properties of the 12 stable *S*-XS_2 monolayers (X = Si, Ge, Sn, Pb, Ti, V, Cr, Mn, Zr, Mo, Re, and Os) (Table 1). The mechanical properties associated with elastic constants (C_{11}, C_{12}, C_{22} and C_{66}) can be described by two independent parameters, the orientation-dependent Young's moduli $Y(\theta)$ and Poisson's ratio $v(\theta)$, which can be expressed as follows:[74]

$$Y(\theta) = \frac{C_{11}C_{22} - C_{12}^2}{C_{11}\sin^4\theta + A\sin^2\theta\cos^2\theta + C_{22}\cos^4\theta} \qquad \text{(Equation 2)}$$

$$\nu(\theta) = \frac{C_{12}\sin^4\theta - B\sin^2\theta\cos^2\theta + C_{12}\cos^4\theta}{C_{11}\sin^4\theta + A\sin^2\theta\cos^2\theta + C_{22}\cos^4\theta} \qquad \text{(Equation 3)}$$

where $A = (C_{11}C_{22} - C_{12}^2)/C_{66} - 2C_{12}$, $B = C_{11} + C_{12} - (C_{11}C_{22} - C_{12}^2)/C_{66}$.

Table 1 The elastic constants (in Nm^{-1}), Young's moduli Y (in Nm^{-1}), and Poisson's ratio v of the 12 stable *S*-XS_2 structures. The NPRs are highlighted in bold.

	C_{11}	C_{22}	C_{12}	C_{66}	Y_x	Y_y	ν_x	ν_y
S-SiS_2	96.37	96.37	−5.18	2.13	96.09	96.09	**−0.054**	**−0.054**
S-GeS_2	75.55	75.55	−4.73	1.72	75.25	75.25	**−0.063**	**−0.063**
S-SnS_2	51.39	51.39	−4.27	0.98	51.04	51.04	**−0.083**	**−0.083**
S-PbS_2	39.49	39.49	−2.45	0.09	39.34	39.34	**−0.062**	**−0.062**
S-TiS_2	31.38	31.38	0.51	5.05	31.37	31.37	0.016	0.016
S-VS_2	28.55	28.55	3.38	7.49	28.15	28.15	0.118	0.118
S-CrS_2	40.30	40.30	10.91	11.31	37.35	37.35	0.271	0.271
S-MnS_2	42.33	42.33	10.85	10.85	39.55	39.55	0.256	0.256
S-ZrS_2	29.70	29.70	0.44	1.78	29.69	29.69	0.015	0.015
S-MoS_2	44.10	44.10	12.71	8.54	40.44	40.44	0.288	0.288
S-ReS_2	29.96	29.96	11.82	9.71	25.30	25.30	0.395	0.395
S-OsS_2	37.47	37.47	15.20	2.66	31.30	31.30	0.406	0.406

Based on the above equations, we plotted the variations of Y and v with respect to the angle θ in Fig. 2. It is found that the in-plane Young's moduli of these 12 *S*-XS_2 monolayers are all small (less than 96.09 Nm^{-1}) and anisotropic (Fig. 2a and b). The highest values of in-plane Young's moduli are observed along the *x*/*y*-direction, while the lowest values are along with $\theta = 45°\times n$ (n = 1, 2, 3, 4) directions. Particularly, the *S*-ReS_2 monolayer exhibits a reversal in the largest and lowest Y values with respect to θ. For *S*-SiS_2/*S*-ReS_2, the maximum/minimum value of Young's moduli is 96.09/25.30 Nm^{-1}. Nevertheless, these values are all smaller than that of graphene (342.2 Nm^{-1}),[75] and hexagonal MoS_2 monolayer (120 Nm^{-1}),[76] indicating their promising applications as flexible devices.

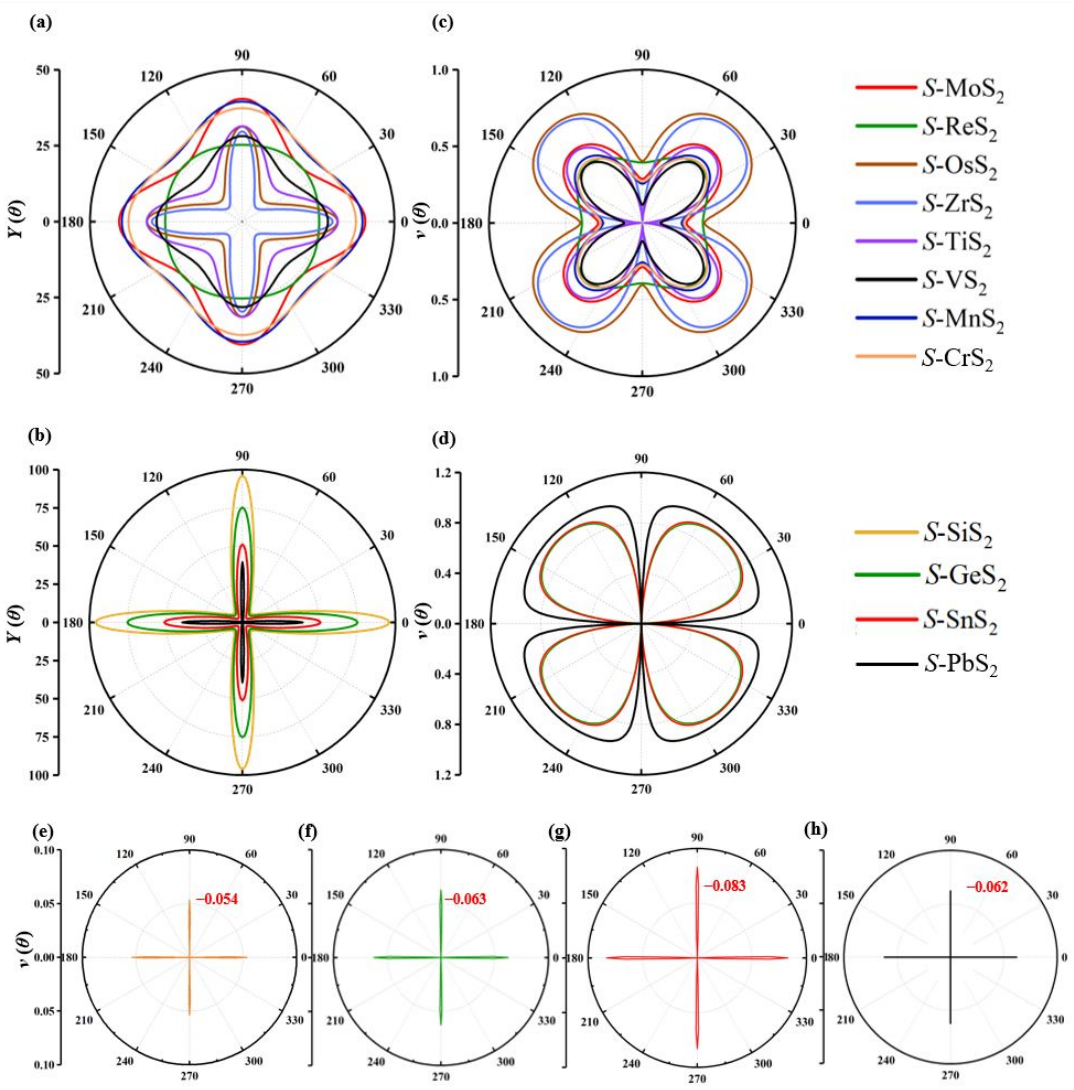

Fig. 2 Orientation-dependent in-plane Young's moduli $Y(\theta)$ and Poisson's ratio $v(\theta)$ for the *S*-XS_2 monolayers: (a, c) X = Mo, Re, Os, Zr, Ti, V, Cr, Mn, and (b, d) X = Si, Ge, Sn, and Pb. (e~h) NPRs for *S*-XS_2 (X = Si, Ge, Sn, and Pb).

The Poisson's ratios of the *S*-XS_2 monolayers are shown in Fig. 2c and d, ranging from −0.083 to 0.94. All structures have their highest Poisson's ratios along with the θ = 45°×n (n = 1, 2, 3, 4) directions, while the lowest Poisson's ratios are observed along the *x*- and *y*-directions. According to Frantsevich's rule,[77] materials with Poisson's ratio smaller/larger than 1/3 exhibit brittle/ductile mechanical properties, respectively. Thus,

the *S*-XS_2 (X = Ti, V, Cr, Mn, Zr, and Mo) monolayers possess a brittle character, whereas *S*-XS_2 (X = Re and Os) monolayers show ductility.

Notably, the four main group-based *S*-XS_2 monolayers (X = Si, Ge, Sn, and Pb) possess negative Poisson's ratios (NPRs), suggesting their exceptional mechanical properties, such as resistance to denting,[78] high fracture toughness,[79] and outstanding vibration or sound absorption capabilities.[80] Besides, the NPR values of the *S*-SiS_2, *S*-GeS_2, *S*-SnS_2, and *S*-PbS_2 (−0.054, −0.063, −0.083, and −0.062, respectively, see Fig. 2e~h) are more negative than those of *δ*-phosphorene (−0.027),[81] and borophene (−0.022),[82] which suggests that these four square disulfide monolayers exhibit a more pronounced response as auxetic material.

Materials with NPRs exhibit a fascinating auxetic effect, where they can be simultaneously stretched or compressed in two directions. To validate the NPRs property of the *S*-SiS_2, *S*-GeS_2, *S*-SnS_2, and *S*-PbS_2 monolayers, we examined the cross-sectional response under uniaxial strains (δ) ranging from −6% to 6% along the *x*-direction due the square configuration (Fig. S7). The strain δ was defined as $\delta = (l - l_0)/l_0$, where $l = a$ represents the strained lattice length along the *x*-direction, $l_0 = a_0$ is the corresponding lattice constant without strain.

As expected, we found that as the uniaxial strain δ_x varies from −6% to 6%, the response in the *y*-direction (δ_y) increases monotonically: −0.38%~0.40% for *S*-SiS_2, −0.38%~0.40% for *S*-GeS_2, −0.26%~0.37% for *S*-SnS_2, −0.36%~0.35% for *S*-PbS_2, respectively. Thus, when the lattice is compressed/stretched along the *x*-axis, the lattice length along the *y*-axis undergoes compression/stretching simultaneously, confirming

that the *S*-SiS_2, *S*-GeS_2, *S*-SnS_2, and *S*-PbS_2 monolayers possess the NPR properties. Note that, the NPR behavior has also been found in the penta-MS_2,[83] *S*-SN_2 [21] and square-A_2B (A = Cu, Ag, Au, and B = S, Se) monolayers.[84]

3.4 Magnetic and electronic properties

Before examining the band structures of the 12 stable *S*-XS_2 (X = Si, Ge, Sn, Pb, Ti, V, Cr, Mn, Zr, Mo, Re, and Os) monolayers, we conducted an analysis of their magnetic properties. The DFT+U approach, which is typically used to treat the strong electron correlation in transition metals, was employed to obtain the ground state energies of *S*-XS_2 monolayers. U_{eff} = U–J = 3 eV was used for transition metal atoms based on previous studies on related systems such as $Cr_2TiC_2F_2$,[85] VI_3,[86] Cr_2N,[87] $Mo_3N_2F_2$,[88] and Mn_2CF_2.[89] Besides the nonmagnetic state, three magnetic configurations, namely, ferromagnetic (FM), and two antiferromagnetic states (AFM1 and AFM2), were considered (Fig. S8).

We found that the *S*-VS_2, *S*-CrS_2, and *S*-MnS_2 monolayers are ferromagnetic (FM), while *S*-MoS_2 is antiferromagnetic (AFM1), in which the metal atom carries the magnetic moment of 1.39, 2.91, 3.28, and ±1.46 μ_B for V, Cr, Mn, and Mo, respectively (Fig. S9). The remaining eight *S*-XS_2 monolayers show nonmagnetic behavior. We have also calculated the lattice constants for these new magnetic ground state configurations (see Table S5), for the antiferromagnetic *S*-MoS_2, the lattice constant is only doubled, while for the ferromagnetic *S*-VS_2, *S*-CrS_2 and *S*-MnS_2, the lattice

constants increase slightly (by 0.12, 0.16 and 0.31 Å, respectively) due to the interaction of magnetic atoms.

Then we evaluated the Curie temperature (T_c) of three ferromagnetic structures, *i.e.*, the *S*-VS_2, *S*-CrS_2, and *S*-MnS_2 monolayers, by both mean-field theory (MFT)[90] and Monte Carlo (MC) simulations based on the Ising model. The nearest and next-nearest neighboring coupling of on-site spin (S) were considered, the Hamiltonian of the system can be expressed as:

$$H = H_0 - \sum_{i,j} J_1 S_i S_j - \sum_{k,l} J_2 S_k S_l$$

where H_0 is the energy of the non-magnetic state, J_1/J_2 is the nearest/next-nearest exchange coupling parameters; and $S = MS_0$, M is the on-site magnetic moments for transition metal, S_0 = 1/2. To calculate J_1 and J_2, we adopted the three magnetic configurations in Fig. S8. For the AFM1, AFM2, and FM states, the energy can be written as:

$$H_{(A)} = H_0 + 8J_2S^2$$
$$H_{(B)} = H_0 + 8J_1S^2 - 8J_2S^2$$
$$H_{(C)} = H_0 - 8J_1S^2 - 8J_2S^2$$

Table 2 summarizes the calculated values of exchange coupling parameters (J_1 and J_2) and the estimated Curie temperatures (T_c^{MFT} and T_c^{MC}) of the *S*-VS_2, *S*-CrS_2, and *S*-MnS_2 monolayers. The on-site magnetic moments of transition metal atoms in these monolayers from MC simulations are plotted as a function of temperature in Fig. S10. We also calculated the Curie temperature of CrI_3 monolayer to check the accuracy of our calculations. Obviously, for CrI_3 monolayer, the Curie temperature obtained by MC method overestimates by 2~3 times (130 K), this is the downside of the Ising model,

while the MFT method (47.48 K) agreed well with the theoretical (46.4 K)[90] and experimental values (45 K).[91] Nevertheless, by equation $T_c = \frac{2JS^2}{3K_B}$, the MFT-predicted Curie temperatures for our structures are 202.66 K for *S*-VS_2, 879.34 K for *S*-CrS_2, and 439.07 K for *S*-MnS_2. Our results are comparable to or even higher than recent study of 2H-VSSe monolayer (346 K).[92]

Additionally, we investigated the easy axis (EA) of the ferromagnetic *S*-VS_2, *S*-CrS_2 and *S*-MnS_2 monolayers, and found that it aligns along the (001) direction. Note that it is structurally isotropic in the in-plane (*xy*) direction for the square monolayers, and thus there is a magnetic anisotropy energy (MAE) only in the *xz* or *yz* direction. The MAE for these monolayers is significantly high, 0.028, 0.144, and 0.145 meV, respectively (see Fig. 3). These values are much higher than those of some 2D ferromagnetic materials, such as $CrCl_3$ (0.025 meV)[93] and CrF_3 (0.119 meV).[94]

Table 2 On-site magnetic moments (M) for transition metal, exchange coupling parameters (J_1 and J_2), and Curie temperature (T_c^{MFT} and T_c^{MC}) of *S*-VS_2, *S*-CrS_2, *S*-MnS_2 and CrI_3 monolayer. The data in italic were taken from Ref. 90.

	M (μ_B)	J_1 (meV)	J_2 (meV)	T_c^{MFT} (K)	T_c^{MC} (K)
S-VS_2	1.39	54.28	6.28	202.66	730
S-CrS_2	2.91	53.73	2.47	879.34	3100
S-MnS_2	3.28	21.12	1.26	439.07	1600
CrI_3	3.00	2.73/*2.70*	0.53	47.48/*46.4*	130

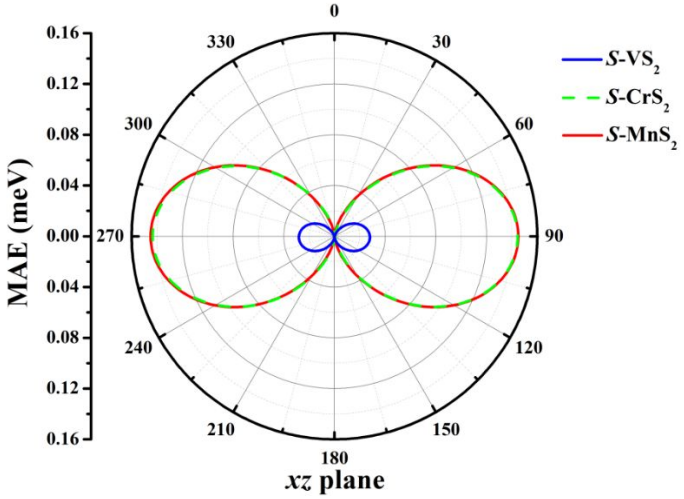

Fig. 3 Angular dependence of MAE in the ferromagnetic system for *S*-VS_2, *S*-CrS_2, and *S*-MnS_2 monolayers lying on *xz* plane.

To gain a deeper understanding of the electronic structures of the *S*-XS_2 monolayers, we analyzed the atom-projected band structures (Fig. 4). Since the PBE functional tends to underestimate the band gap, we used the HSE06 method to obtain more accurate band gap values (E_{gap}).

Among the 12 stable monolayers, three *S*-XS_2 monolayers, namely, *S*-MoS_2, *S*-ReS_2, *S*-OsS_2 (Fig. 4a~c), are metallic. In comparison, six *S*-XS_2 monolayers are semiconductors (Fig. 4d~i), with *S*-TiS_2, *S*-ZrS_2, *S*-SiS_2, *S*-GeS_2, *S*-SnS_2, and *S*-PbS_2 displaying indirect band gaps (2.15, 2.79, 2.77, 2.57, 2.59, and 1.59 eV, respectively, see Table 3).

Remarkably, the ferromagnetic *S*-VS_2 monolayer (Fig. 4j and k) has a direct/indirect band gap (1.07/3.26 eV) in the spin-up/down channel and is featured as a half-semiconductor semiconductor, since it is a semiconductor in one spin channel but insulator in the other spin channel.[95] This unique characteristic enables the generation

and manipulation of spin currents, making it a promising material for spintronic applications.

Furthermore, the ferromagnetic *S*-CrS_2 and *S*-MnS_2 monolayers (Fig. 4l~o) exhibit half-metallic characteristics, where the spin-up channel behaves as a metal, and the spin-down channel acts as a semiconductor (band gap of 3.44 and 4.23 eV, respectively), leading to 100% spin polarization in the respective spin channels.[96]

For comparison, our computed results of the *S*-GeS_2 monolayer agree well with the reported values of the t-GeS_2 sheet, as both materials have the same structure).[97] Specifically, we observe close agreement in terms of lattice constant (3.51 *vs* 3.49 Å), PBE/HSE06 band gap (1.42 *vs.* 1.39 eV/2.60 *vs.* 2.57 eV). This consistency underscores the reliability of our computational approach.

Table 3 HSE06 band gaps (E_{gap}, eV), positions of VBM and CBM of nonmagnetic *S*-XS_2 (X = Ti, Zr, Si, Ge, Sn, and Pb), spin up and spin down channels of ferromagnetic *S*-XS_2 (X = V), and spin down channel of half-metallic *S*-XS_2 (X = Cr and Mn) monolayers. The PBE values were compared in italic.

	S-TiS_2	*S*-ZrS_2	*S*-SiS_2	*S*-GeS_2	*S*-SnS_2	*S*-PbS_2	*S*-VS_2 (up/down)	*S*-CrS_2 (down)	*S*-MnS_2 (down)
E_{gap}	2.15	2.79	2.77	2.57	2.59	1.59	1.07/3.26	3.48	4.23
	1.28	*1.89*	*1.70*	*1.39*	*1.46*	*0.62*	*0.00/1.83*	*2.75*	*2.49*
VBM	−7.08	−7.14	−6.33	−6.38	−6.73	−6.79	−6.69/−7.25	--	--
	Γ	Γ	X	X	X	X	Γ/Γ	Γ	X
CBM	−4.93	−4.35	−3.56	−3.81	−4.14	−5.20	−5.62/−3.99	--	--
	S-Γ indirect	S-Γ indirect	Γ indirect	Γ indirect	Γ indirect	Γ indirect	Γ/S direct/indirect	S indirect	S indirect

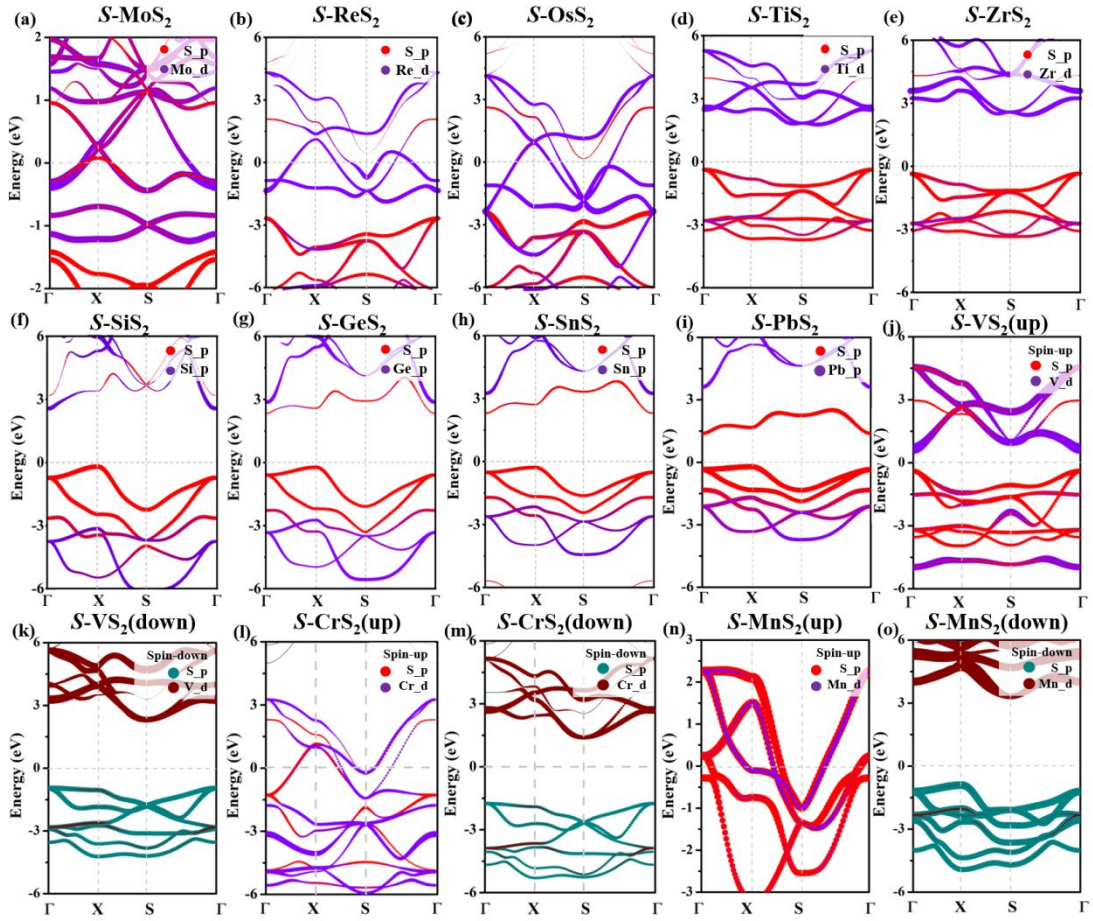

Fig. 4 Atom-projected band structures of the *S*-XS_2 monolayers calculated by HSE06 functional. (a) *S*-MoS_2. (b) *S*-ReS_2. (c) *S*-OsS_2. (d) *S*-TiS_2. (e) *S*-ZrS_2. (f) *S*-SiS_2. (g) *S*-GeS_2. (h) *S*-SnS_2. (i) *S*-PbS_2. (j) *S*-VS_2 (spin-up). (k) *S*-VS_2 (spin-down). (l) *S*-CrS_2 (spin-up). (m) *S*-CrS_2 (spin-down). (n) *S*-MnS_2 (spin-up). (o) *S*-MnS_2 (spin-down).

Specifically, for *S*-TiS_2 and *S*-ZrS_2 sheets, the valence band maximum (VBM) and conduction band minimum (CBM) are located at Γ point and between the S and Γ points, and are dominated by the S_p and Ti/Zr_d orbitals (Fig. 4d and e), respectively. As for the ferromagnetic *S*-VS_2 monolayer, the VBM and CBM position are located at the Γ (Γ) point and Γ (S) in spin-up (spin-down) channel, respectively. These states are primarily attributed to the S_p and V_d orbitals (Fig. 4j and k), respectively. For the

semiconducting *S*-SiS_2, *S*-GeS_2, *S*-SnS_2, and *S*-PbS_2 structures, the VBM/CBM is located at X/Γ point, and the contribution mainly comes from the S_p/S_p and Si/Ge/Sn/Pb_p orbitals (Fig. 4f~i).

Furthermore, we computed the partial charge of semiconductors at the VBM and CBM for the lowest magnetic state (Fig. S11). These computations confirm that the contributions of the VBM and CBM for each *S*-XS_2 monolayer agree well with the results obtained from the atom-project band structures.

3.5 Carrier mobility

Understanding the electronic transport properties is essential for us to explore the potential applications of 2D materials for future electronics.[98] In this regard, we investigated the transport properties of the semiconducting *S*-XS_2 (X = Si, Ge, Sn, Pb, Zr, Ti, and V) monolayers by employing the deformation potential theory[99] to calculate the carrier mobility, which was determined using the following equation:

$$\mu = \frac{e\hbar^3 C_{2D}}{k_B T m^* m_d^* E_l^2} \qquad \text{(Equation 4)}$$

in which e, $\hbar$ and k_B are constants, representing the electron charge, reduced Planck constant, and the Boltzmann constant; T is the room temperature (300 K); C_{2D} is the 2D elastic moduli, which is defined as $C_{2D} = (\partial^2 E/\partial\delta^2)/S_0$, where E and S_0 represent the total energy and surface area of the equilibrium system; m^* is the effective mass in the transport (both x and y) direction and $m_d^* = \sqrt{m_x^* m_y^*}$ is the average carrier effective mass; E_l is the deformation potential (DP) constant obtained from the equation $E_l = \partial E_{edge}/\partial\varepsilon$, where E_{edge} is the value of valence band maximum (VBM) and conduction

band minimum (CBM), the uniaxial strain range we investigated is from −1.5% to 1.5% with the steps of 0.5%, and fitting curves are shown in Fig. S12. All these data were computed at the HSE06 level, and the corresponding values are listed in Table 4. To examine the accuracy of our calculation method, the mobility of black phosphorus (BP) monolayer with an orthorhombic lattice was also calculated, and our results are in line with the values reported in Ref. 100.

In our analysis, we chose the *x*-direction as the transport direction and considered both spin-up and spin-down channels for the ferromagnetic *S*-VS_2. Our calculations revealed that all seven semiconducting monolayers have moderate electron mobilities (Table 4), ranging from 29.05 to 239.59 $cm^2V^{-1}s^{-1}$, which are comparable to or higher than the electron mobility of the hexagonal MoS_2 monolayer (77.30 $cm^2V^{-1}s^{-1}$).[101] Notably, Xu *et al.* successfully prepared 2D SnS_2 with a hexagonal structure and found that the electron mobility at room temperature is about 2.58 $cm^2V^{-1}s^{-1}$,[102] which is an order of magnitude lower than our findings for the square configuration (96.50 $cm^2V^{-1}s^{-1}$).

Table 4 Computed effective mass (m^*) of the electron, light hole (*l*-hole), and heavy hole (*h*-hole), elastic constant (C_{2D}), deformation potential constant (E_l), and carrier mobilities (μ) for the *S*-SiS_2, *S*-GeS_2, *S*-SnS_2, *S*-PbS_2, *S*-ZrS_2, *S*-TiS_2, *S*-VS_2 (including both spin-up (*u*) and spin-down (*d*) channels), and black-phosphorus (BP) monolayers. The data in italic are taken from Ref. 100, m_0 is the mass of an electron.

	Carrier type	m^*/m_0	C_{2D} (J m^{-2})	E_l (eV)	μ (cm^2 V^{-1} s^{-1})
S-SiS_2	electron	0.38	96.37	7.71	239.59
	hole	−2.17		7.86	7.07
S-GeS_2	electron	0.41	75.55	9.83	99.26
	hole	−2.73		6.67	4.86
S-SnS_2	electron	0.43	51.39	7.84	96.50
	hole	−3.48		5.67	2.82
S-PbS_2	electron	0.48	39.49	5.84	107.25
	hole	4.61		2.77	5.17
S-ZrS_2	electron	0.67	29.70	2.79	181.38
	h/*l* -hole	−1.87/−0.47		7.45/0.41	3.27/17068.47
S-TiS_2	electron	0.93	31.38	3.52	62.49
	h/*l* -hole	−2.03/−0.44		9.66/0.77	1.74/5834.02
S-VS_2^u	electron	0.49	28.55	4.19	144.54
	h/*l* -hole	−0.71/−0.43		11.84/3.62	8.62/251.45
S-VS_2^d	electron	1.07		4.28	29.05
	h/*l* -hole	−15.18/−0.53		3.61/7.86	0.20/35.11
BP	electron (*x*)	0.15/*0.17*	25.08/*28.94*	3.05/*2.72*	885.80/*~1100*
	hole (*x*)	−0.14/*−0.15*		2.54/*2.50*	630.46/*~640*
	electron (*y*)	1.25/*1.12*	103.65/*101.64*	6.41/*7.11*	99.46/*~80*
	hole (*y*)	−6.31/*−6.35*		0.23/*0.15*	7050.29/*~10000*

For the hole mobilities, the values of the *S*-SiS_2, *S*-GeS_2, *S*-SnS_2, and *S*-PbS_2 monolayers are 7.07, 4.86, 2.82, and 5.17 cm^{2}V^{-1}s^{-1}, respectively. Interestingly, for the *S*-ZrS_2, *S*-TiS_2, and *S*-VS_2 (including both spin-up and spin-down channels) monolayers, VBM exhibits two-fold degeneracy at the Γ point, resulting in two types of holes with different masses, we denoted them as heavy holes (*h*-hole) and light holes (*l*-hole), respectively. As shown in Table 4, there is a significant difference between the mobilities of *h*- and *l*-hole. For example, the *h*-hole mobility of the *S*-ZrS_2 monolayer

is only 3.27 $cm^2V^{-1}s^{-1}$, while the *l*-hole mobility is as high as 17068.47 $cm^2V^{-1}s^{-1}$, due to the lower deformation potential and effective mass of the *l*-hole. Generally speaking, the substantial difference between the electron and hole mobilities in these monolayers is beneficial for effectively separating photogenerated electrons and holes, making these 2D structures promising as light-harvesting materials in photovoltaic cells and photocatalysis.

To explore the relationship between *h*- and *l*-hole, taking the *S*-ZrS_2 monolayer as an example, we applied uniaxial strains (−1.5% and 1.5%) in the *x*-direction and calculated the resulting energy bands (Fig. 5a~c). We specify Γ-X and Γ-Y as the transport directions of *x* and *y*, respectively. Without any strains, the *h*- and *l*- hole bands are degenerate at the Γ point. However, the degeneracy gradually disappears under applied strains. In the *x*-direction, when the *h*-hole band is higher than the *l*-hole band, the presence of larger effective mass and deformation potential result in a lower mobility (3.27 $cm^2V^{-1}s^{-1}$) at $\delta_x = -1.5\%$. In contrast, under the strain of $\delta_x = 1.5\%$, the *l*-hole band becomes higher, leading to a lower effective mass and deformation potential, and consequently, to a higher mobility (17068.47 $cm^2V^{-1}s^{-1}$). Interestingly, the position of its *l*-hole band in the *x*-direction align precisely with the *h*-hole band in the *y*-direction. Therefore, the significant change in carrier mobility induced by uniaxial strain suggests that these materials hold promise for applications in nanosensors.[84]

3.6 Photocatalytic properties

The above analyses showed that six *S*-XS_2 (X = Si, Ge, Sn, Pb, Zr, and Ti) monolayers are semiconducting with band gaps in the range of 1.59~2.79 eV. These band gaps

fulfill the first requirement of a photocatalyst for water-splitting, as they fall within the suitable range of 1.23~3.00 eV. To meet the second requirement for photocatalytic water splitting, it is essential for the band edges of the materials to align with the redox potential of water. However, the redox potential of water is dependent on the pH value of the solutions: the standard reduction potential of H^+/H_2 ($E^{red}(H^+/H_2)$) and the oxidation potential of H_2O/O_2 ($E^{ox}(H_2O/O_2)$) with the inclusion of environmental pH can be described by $E^{red}(H^+/H_2) = -4.44+pH\times0.059$ eV and $E^{ox}(H_2O/O_2) = -5.67+pH\times0.059$ eV, respectively.[83]

To obtain the energies of CBM and VBM, we calculated the work functions sing the formula: $\varphi = E_{vac} - E_F$, where E_{vac} is the energy of a stationary electron in the vacuum nearby the surface, and E_F is the Fermi energy. Thus, we can take φ as the energy of VBM (E_{VBM}), and the energy of CBM can be obtained *via* the expression of $E_{CBM} = E_{VBM} + E_{gap}$, where E_{gap} is the bandgap calculated by HSE06 level of theory (see Table 3).[103] The CBM and VBM energies of the six *S*-XS_2 (X = Si, Ge, Sn, Pb, Zr, and Ti) monolayers at different pH values are presented in Fig. S13.

As shown in Fig. S13b and c, the band edge positions straddle the redox potential for *S*-SiS_2 and *S*-GeS_2 in a neutral environment (pH=7), and for *S*-SiS_2 in an alkaline environment (pH=14). However, there is a significant energy difference ($\Delta E_1/\Delta E_2$) between the CBM/VBM and the reduction/oxidation potential. In a neutral environment, the $\Delta E_1/\Delta E_2$ values for *S*-SiS_2 and *S*-GeS_2 are 0.47/1.07 and 0.22/1.12, respectively; In an alkaline environment, the $\Delta E_1/\Delta E_2$ value for *S*-SiS_2 is 0.05/1.49. This large difference in energy indicates a significant mismatch in the driving force for the redox reaction,

suggesting that these six *S*-XS_2 materials are unsuitable for these specific pH environments.

However, under acidic conditions (pH=0, Fig. S13a), four *S*-XS_2 (X = Si, Ge, Sn, and Zr) monolayers have band edge positions that span the redox potential. However, the significant difference between ΔE_1 and ΔE_2 values of *S*-SnS_2 (0.30 and 1.06 eV) and *S*-ZrS_2 (0.09 and 1.47 eV) suggests that these two monolayers are not ideal photocatalysts. On the other hand, for *S*-SiS_2 and *S*-GeS_2, the $\Delta E_1/\Delta E_2$ values are 0.88/0.66 and 0.63/0.71 eV, respectively, indicating comparable driving forces for the oxidation and reduction reactions. Thus, both *S*-SiS_2 and *S*-GeS_2 monolayers have the potential to be effective photocatalysts for water splitting. Further calculations revealed that the redox reactions are best driven at pH values of 2 and 0 for *S*-SiS_2 and *S*-GeS_2 (the $\Delta E_1/\Delta E_2$ is 0.76/0.78 and 0.63/0.71 eV, respectively), respectively, as shown in Fig. 5d.

The optical absorption properties of the photocatalyst play a vital role in the entire water-splitting process, and an efficient photocatalyst should be able to absorb visible and ultraviolet light.[11] Thus, we further investigated the absorption spectra of the *S*-SiS_2 and *S*-GeS_2 monolayers using the complex dielectric constants (ε) at a given frequency with the HSE06 hybrid functional.[104] As illustrated in Fig. 5e, both *S*-SiS_2 and *S*-GeS_2 exhibit considerable absorption coefficients (up to the order of 10^3 and 10^4 cm^{-1}, respectively) in the visible-light region. Moreover, their absorption coefficients in the ultraviolet region are much stronger, reaching values up to the order of 10^6 cm^{-1}. The high absorption coefficients in both visible and ultraviolet light indicate that the *S*-SiS_2

and *S*-GeS_2 monolayers possess efficient light harvesting capabilities, making them favorable candidates for photocatalyzing water splitting.

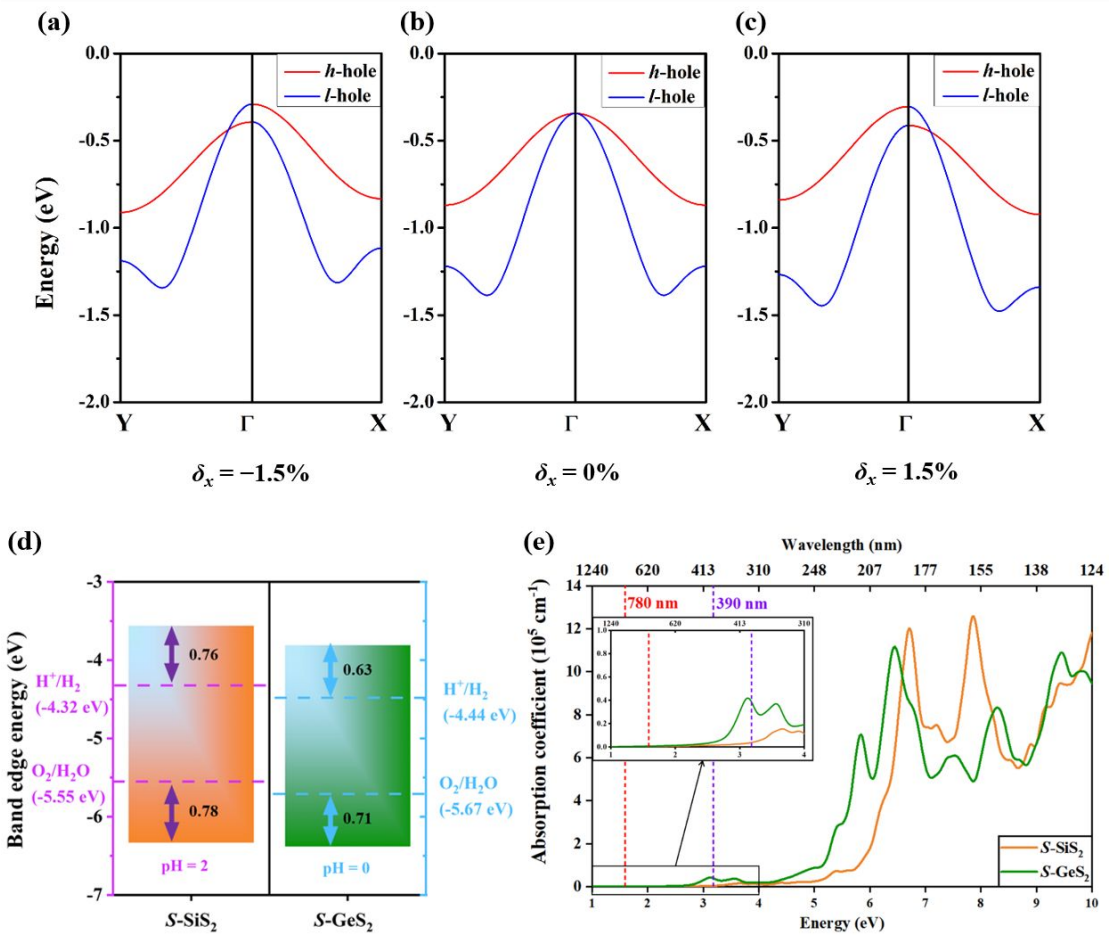

Fig. 5 The *h*- and *l*-hole bands of *S*-ZrS_2 monolayer under the *x*-axial strains of (a) −1.5%, (b) 0%, and (c) 1.5%. (d) The alignment band edge of *S*-SiS_2 and *S*-GeS_2 monolayer and water redox potentials at pH value equal to 2 and 0, respectively. (e) Optical absorption spectra of *S*-SiS_2 and *S*-GeS_2 monolayers at the HSE06 level of theory. The inset is a zoomed view of the absorption spectra in the visible light range.

3.7 Electrochemical Catalytic performance towards HER

From the electronic properties discussed before, the *S*-CrS_2 *S*-MnS_2, *S*-MoS_2, *S*-ReS_2, and *S*-OsS_2 monolayers have been confirmed to have metallic feature, which endows them applicable as electrocatalysts for hydrogen evolution reaction (HER) since the good conductivity can improve the efficiency and minimize energy loss caused by resistance in the electrochemical process.

To examine the capability of the five metallic *S*-XS_2 (X = Cr, Mn, Mo, Re, and Os) monolayers as electrocatalysts for HER, we calculated the Gibbs free energy of the adsorbed hydrogen atom ($\Delta G_{*\mathrm{H}}$, * refers the catalyst).[105]

First, the HER pathway under standard condition is characterized as follows:

$$\mathrm{H}^+(\mathrm{aq}) + \mathrm{e}^- \rightarrow \frac{1}{2}\mathrm{H}_2(\mathrm{g});\ \Delta G^0 = 0\ \mathrm{eV} \qquad \text{(Equation 5)}$$

The total energies of the reactants and the products are equal, thus, the $\Delta G_{*\mathrm{H}}$ is a crucial descriptor to detect the HER catalytic activity of a catalyst, as defined in Eq. (6).

$$\Delta G_{*\mathrm{H}} = \Delta E_{\mathrm{H}} + \Delta E_{\mathrm{ZPE}} - T\Delta S_{\mathrm{H}} \qquad \text{(Equation 6)}$$

where the ΔE_{H} is the adsorption energy of H calculated by Equation (7), ΔE_{ZPE} and $T\Delta S_{\mathrm{H}}$ are the difference in zero-point energy and the entropy between H adsorption and hydrogen in the gas phase, respectively, which can be obtained by Equations (8) and (9).

$$\Delta E_{\mathrm{H}} = E_{\mathrm{H}^*} - E_* - \frac{1}{2}E_{\mathrm{H}_2} \qquad \text{(Equation 7)}$$

where E_{H^*}, E_* and E_{H_2} denote the energy of catalyst with adsorbing H, the energy of catalyst, and the energy of gas phase H_2, respectively.

$$\Delta E_{\mathrm{ZPE}} = E_{\mathrm{ZPE}}^{\mathrm{H}} - E_{\mathrm{ZPE}} - \frac{1}{2}E_{\mathrm{ZPE}}^{\mathrm{H}_2} \qquad \text{(Equation 8)}$$

where $E_{\mathrm{ZPE}}^{\mathrm{H}}/E_{\mathrm{ZPE}}$ is the zero-point energy of the *S*-XS_2 (X = Mo, Re, Os, Mn) with/without absorbing H, $E_{\mathrm{ZPE}}^{\mathrm{H_2}}$ is the zero-point energy of gas phase H_2.

$$\Delta S_{\mathrm{H}} \approx -\frac{1}{2} S_{\mathrm{H_2}}^{0} \qquad \text{(Equation 9)}$$

where $S_{\mathrm{H_2}}^{0}$ represents the entropy of H_2 under standard conditions.

According to the benchmark reference, a theoretical $\Delta G_{*\mathrm{H}}$ value of −0.09 eV for Pt electrocatalyst at H coverage (θ) of 1/4,[106] typically a material satisfying $|\Delta G_{*\mathrm{H}}| < 0.09$ eV is regarded as a promising electrocatalyst for HER. In this work, we set the critical condition as $|\Delta G_{*\mathrm{H}}| < 0.20$ eV. The $\Delta G_{*\mathrm{H}}$ value is dependent on the adsorption of H. For the nonmagnetic *S*-ReS_2, *S*-OsS_2 and ferromagnetic *S*-CrS_2, *S*-MnS_2 monolayers, we considered eight adsorption sites (S1-S8, Fig. S14a). Additionally, for the antiferromagnetic *S*-MoS_2 monolayer, we examined five more adsorption sites (S1-S13, Fig. S14b). The $\Delta G_{*\mathrm{H}}$ values at the considered adsorption sites on the *S*-ReS_2, *S*-OsS_2, *S*-CrS_2, *S*-MnS_2, and *S*-MoS_2 monolayers of a 2×2×1 supercell (containing four X atoms, the θ is 1/4) are presented in Table S6 and Table S7.

The nonmagnetic monolayers, specifically *S*-ReS_2 and *S*-OsS_2, exhibit optimal $\Delta G_{*\mathrm{H}}$ values (0.17 and 0.46 eV for respectively) at the S5 site. On the other hand, the ferromagnetic *S*-CrS_2, *S*-MnS_2, and antiferromagnetic *S*-MoS_2 monolayers have optimal $\Delta G_{*\mathrm{H}}$ values all at S8 site (−0.37, −0.49, and 0.23 eV, respectively; see Fig. 6a and Fig. S15a). However, only the $\Delta G_{*\mathrm{H}}$ value of the *S*-ReS_2 monolayer at an H coverage of 1/4 falls within the critical range.

Since the $\Delta G_{*\mathrm{H}}$ is related to the H coverage, we further constructed and relaxed 3×3×1 (θ = 1/9) and 4×4×1 (θ = 1/16) supercells for the nonmagnetic *S*-XS_2 (X = Re

and Os), ferromagnetic *S*-XS_2 (X = Cr and Mn) monolayers, and 4×4×1 (θ = 1/16) supercell for the antiferromagnetic *S*-MoS_2 monolayer, to examine their catalytic performance (Fig. S15 b and c).

Our calculations revealed that as the H coverage decreases from 1/4 to 1/9, the $\Delta G_{*\mathrm{H}}$ values of *S*-ReS_2, *S*-OsS_2, *S*-CrS_2, and *S*-MnS_2 decrease to −0.06, 0.03, −0.38, and −0.50 eV, respectively. Similarly, when θ = 1/16, the $\Delta G_{*\mathrm{H}}$ values of *S*-ReS_2, *S*-OsS_2, *S*-CrS_2, *S*-MnS_2, and *S*-MoS_2 decrease to −0.18, −0.09, −0.41, −0.52, and 0.09 eV, respectively (see Fig. 6b),

In addition to the analysis of the catalytic performance, we also performed magnetic tests on the systems after H adsorption and recalculated the corresponding $\Delta G_{*\mathrm{H}}$ values (see Table S8). Interestingly, we found that only the magnetism of *S*-MoS_2 transformed into a ferromagnetic (FM) state upon H adsorption. However, the resulting $\Delta G_{*\mathrm{H}}$ values for *S*-MoS_2 exceed our critical value (from 0.23/0.09 to 0.37/0.32 at low/high H coverage). Thus implying that *S*-MoS_2 is not suitable as a material for HER in terms of its catalytic properties.

Obviously, at the low or medium H coverage (θ = 1/16 or 1/9), the *S*-XS_2 (X = Re and Os) monolayers can boost the HER; while at high H coverage (θ = 1/4), only *S*-ReS_2 monolayer shows promise for HER.

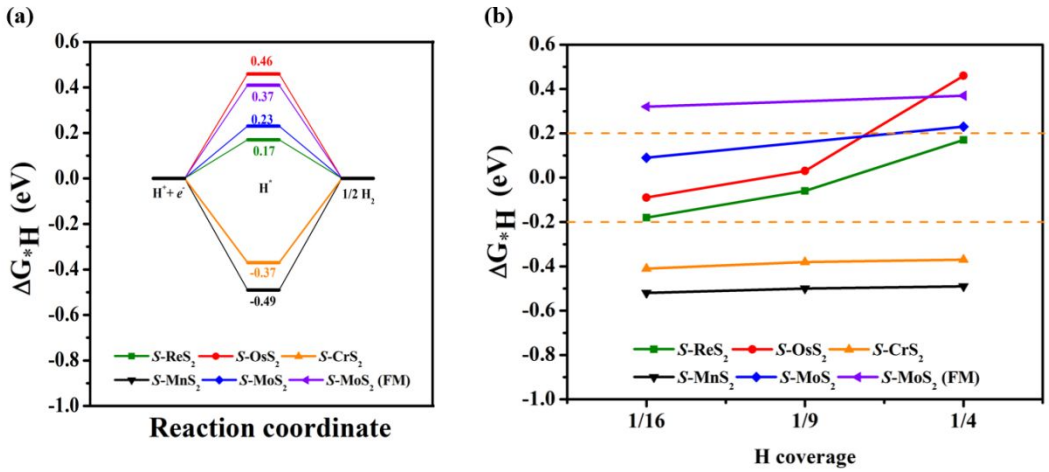

Fig. 6 Calculated $\Delta G_{*\mathrm{H}}$ values of *S*-ReS_2, *S*-OsS_2 *S*-MoS_2, and *S*-MnS_2 monolayers. (a) A 2×2×1 supercell with H coverage of 1/4. (b) Different H coverages, where two orange lines indicate the HER catalyst activity criteria ($|\Delta G_{*\mathrm{H}}|$< 0.20 eV).

4. Conclusion

Using comprehensive first-principles calculations, we theoretically identified 12 stable monolayers (*S*-XS_2 with X = Si, Ge, Sn, Pb, Ti, V, Cr, Mn, Zr, Mo, Re, and Os) featuring unique the previously overlooked square lattice. Specifically, we investigated their mechanical, electronic, and magnetic properties, and explored their applications as photocatalysts and electrocatalysts for green hydrogen production, as summarized in Fig. 7.

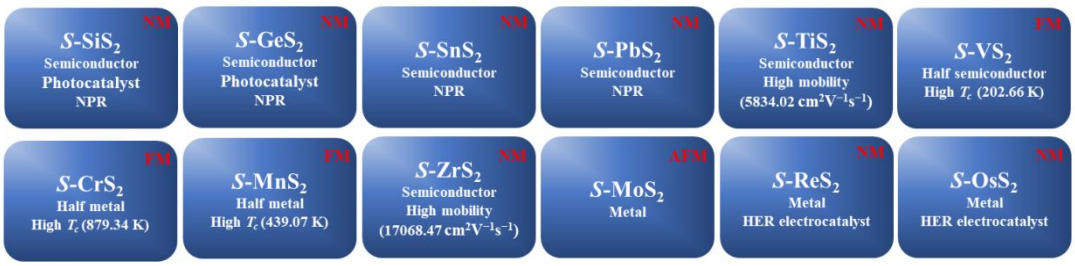

Fig. 7. Properties and application aspects of our 12 stable *S*-XS_2 (X = Si, Ge, Sn, Pb, Ti, V, Cr, Mn, Zr, Mo, Re, and Os) monolayers.

All 12 *S*-XS_2 monolayers have low in-plane Young's modulus (25.30~96.09 Nm^{-1}), and four (*S*-XS_2 with X = Si, Ge, Sn, Pb) exhibit negative Poisson's ratios. These monolayers have diverse magnetic and electronic properties, being nonmagnetic and metallic (*S*-ReS_2 and *S*-OsS_2), antiferromagnetic and metallic (*S*-MoS_2), nonmagnetic and semiconducting (*S*-SiS_2, *S*-GeS_2, *S*-SnS_2, *S*-PbS_2, *S*-ZrS_2, and *S*-TiS_2), ferromagnetic half-semiconducting (*S*-VS_2), and ferromagnetic half-metallic (*S*-CrS_2 and *S*-MnS_2), which are significantly different from typical 2D hexagonal TMD materials with considerable band gaps. The carrier mobilities of the six nonmagnetic semiconductors range from 0.20 to 17068.47 $cm^2V^{-1}s^{-1}$, varying significantly between electrons and holes. Notably, *S*-ZrS_2, *S*-TiS_2, and *S*-VS_2 exhibit two types of holes, *h*-hole and *l*-hole, with hole mobilities modifiable through uniaxial strains. Three XS_2 monolayers (X = V, Cr, and Mn) have high Curie temperatures and magnetic anisotropy energies. The semiconducting *S*-SiS_2 and *S*-GeS_2 monolayers are potential photocatalysts for photocatalytic water splitting due to suitable band gaps, band edge positions, and considerable optical absorption in the visible and ultraviolet regions, while the metallic *S*-ReS_2 and *S*-OsS_2 monolayers show promise as electrocatalysts for HER at specific H coverages.

Despite some stable *S*-XS_2 monolayers having lower cohesive energies than their hexagonal counterparts, there is still potential for synthesizing the square 2D disulfides through suitable methods. For instance, Liu and coworkers successfully synthesized unconventional hexagonal FeSe thin films, contrasting the typical tetra-FeSe monolayer structure.[107] Given the significant advancements in synthesizing large-area 2D

materials[65,66,108] and the exceptional stability and properties demonstrated by the square *S*-XS_2 monolayers, we anticipate that our research will stimulate experimental efforts in fabricating these novel 2D disulfides. Furthermore, we believe it will also encourage further investigations to explore their specific properties and potential applications in various fields.

Supplemental Information

Supplemental information can be found online at https://pubs.acs.org/journal/jmcack.

Acknowledgments

This work was supported in China by the National Natural Science Foundation of China (11828401, 11964024) and the "Grassland Talents" project of Inner Mongolia autonomous region (12000-12102613), and in the USA by NSF-CREST Center for Innovation, Research, and Education in Environmental Nanotechnology (CIRE2N) (Grant Number HRD-1736093). The computational support from the PARATEAR at Guangzhou Supercomputer Center was acknowledged.

Author Contributions

The initial idea was developed by F.L. Y.L. and W.L. performed the calculations under F.L.'s supervision. All authors participated in the data analysis and writing and reading of the paper. F.L. and Z.C. managed the project.

Declaration Of Interests

The authors declare no competing interests.

References

1 K. S. Novoselov, A. K. Geim, S. V. Morozov, D. Jiang, Y. Zhang, S.V. Dubonos, I. V. Grigorieva and A. A. Firsov, Electric field effect in atomically thin carbon films, *Science*, 2004, **306**, 666−669.

2 Q. Tang, Z. Zhou and Z. Chen, Graphene-related nanomaterials: tuning properties by functionalization, *Nanoscale*, 2013, **5**, 4541−4583.

3 S. Z. Butler, S. M. Hollen, L. Cao and Y. Cui, Progress, challenges, and opportunities in two-dimensional materials beyond graphene, *ACS Nano*, 2013, **7**, 2898–2926.

4 Q. Tang, Z. Zhou and Z. Chen, Innovation and discovery of graphene-like materials via density-functional theory computations, *Wiley Interdiscip. Rev. Comput. Mol. Sci.*, 2015, **5**, 360–379.

5 K. Khan, A. K. Tareen, M. Aslam, R. Wang, Y. Zhang, A. Mahmood, Z. Ouyang, H. Zhang and Z. Guo, Recent developments in emerging two-dimensional materials and their applications, *J. Mater. Chem. C*, 2020, **8**, 387–440.

6 P. Miró, M. Audiffred and T. Heine, An atlas of two-dimensional materials, *Chem. Soc. Rev.*, 2014, **43**, 6537−6554.

7 Y. Wang, J. C. Kim, Y. Li, K. Y. Ma, S. Hong, M. Kim, H. S. Shin, H. Y. Jeong and M. Chhowalla, P-type electrical contacts for 2D transition-metal dichalcogenides, *Nature*, 2022, **610**, 61–66.

8 J. M. Klan, D. K. Harper, J. P. Ruffley, X. Y. Gan, J. E. Millstone and J. K. Johnson, Theoretical study of the impact of vacancies and disorder on the electronic properties of $Cu_{2-x}Se$, *J. Phys. Chem. C*, 2021, **125**, 12324–12332.

9 Y. Li, H. Wang, L. Xie, Y. Liang, G. Hong and H. Dai, MoS_2 nanoparticles grown on graphene: an advanced catalyst for the hydrogen evolution reaction, *J. Am. Chem. Soc.*, 2011, **133**, 7296−7299.

10 S. Haldar, H. Vovusha, M. K. Yadav, O. Eriksson and B. Sanyal, Systematic study of structural, electronic, and optical properties of atomic-scale defects in the two-dimensional transition metal dichalcogenides MX_2 (M = Mo, W, X = S, Se, Te), *Phys. Rev. B*, 2015, **92**, 235408.

11 M. R. Ashwin Kishore, K. Larsson and P. Ravindran, Two-dimensional CdX/C_2N (X = S, Se) heterostructures as potential photocatalysts for water splitting: a DFT study, *ACS Omega*, 2020, **5**, 23762−23768.

12 J. Li, Y. Zhang, C. Liu, L. Zheng, E. Petit, K. Qi, Y. Zhang, H. Wu, W. Wang, A. Tiberj, X. Wang, M. Chhowalla, L. Lajaunie, R. Yu and D. Voiry, 3.4% solar-to-ammonia efficiency from nitrate using Fe single atomic catalyst supported on MoS_2 nanosheets, *Adv. Funct. Mater.*, 2022, **32**, 2108316.

13 Y. Xu, M. Kraft and R. Xu, Metal-free carbonaceous electrocatalysts and photocatalysts for water splitting, *Chem. Soc. Rev.*, 2016, **45**, 3039−3052.

14 L. Liao, Q. Zhang, Z. Su, Z. Zhao, Y. Wang, Y. Li, X. Lu, D. Wei, G. Feng, Q. Yu, X. Cai, J. Zhao, Z. Ren, H. Fang, F. Robles-Hernandez, S. Baldelli and J. Bao, Efficient solar water-splitting using a nanocrystalline CoO photocatalyst, *Nat. Nanotechnol.*, 2014, **9**, 69–73.

15 Y. Wang and M. Chhowalla, Making clean electrical contacts on 2D transition metal dichalcogenides, *Nat. Rev. Phys.*, 2022, **4**, 101–112.

16 Z. Gao, X. Dong, N. Li and J. Ren, Novel two-dimensional silicon dioxide with in-plane negative Poisson's ratio, *Nano Lett.*, 2017, **17**, 772−777.

17 S. Zhang, J. Zhou, Q. Wang, X. Chen, Y. Kawazoe and P. Jena, Penta-graphene: a new carbon allotrope, *Proc. Natl. Acad. Sci. U. S. A.*, 2015, **112**, 2372−2377.

18 L. Kou, Y. Ma, C. Tang, Z. Sun, A. Du and C. Chen, Auxetic and ferroelastic

borophane: a novel 2D material with negative Poisson's ratio and switchable Dirac transport channels. *Nano Lett.*, 2016, **16**, 7910−7914.

19 J.-W. Jiang and H. S. Park, Negative Poisson's ratio in single-layer black phosphorus. *Nat. Commun.*, 2014, **5**, 4727.

20 C. Zhang, T. He, S. K. Matta, T. Liao, L. Kou, Z. Chen and A. Du, Predicting novel 2D MB_2 (M = Ti, Hf, V, Nb, Ta) monolayers with ultrafast dirac transport channel and electron-orbital controlled negative Poisson's ratio, *J. Phys. Chem. Lett.*, 2019, **10**, 2567−2573.

21 F. Li, X. Lv, J. Gu, K. Tu, J. Gong, P. Jin and Z. Chen, Semiconducting SN_2 monolayer with three-dimensional auxetic properties: a global minimum with tetracoordinated sulfurs, *Nanoscale*, 2020, **12**, 85–92.

22 L. Yu, Q. Yan and A. Ruzsinszky, Negative Poisson's ratio in 1T-type crystalline two-dimensional transition metal dichalcogenides, *Nat. Commun.*, 2017, **8**, 15224.

23 D. Wu, S. Wang, S. Zhang, J. Yuan, B. Yang and H. Chen, Highly negative Poisson's ratio in a flexible two-dimensional tungsten carbide monolayer, *Phys. Chem. Chem. Phys.*, 2018, **20**, 18924–18930.

24 R. Peng, Y. Ma, Z. He, B. Huang, L. Kou and Y. Dai, Single-layer Ag_2S: a two-dimensional bidirectional auxetic semiconductor, *Nano Lett.*, 2019, **19**, 1227−1233.

25 Z. Li, I. Sami, J. Yang, J. Li, R. V. Kumar and M. Chhowalla, Lithiated metallic molybdenum disulfide nanosheets for high-performance lithium–sulfur batteries, *Nat. Energy*, 2023, **8**, 84–93.

26 D. Xiao, G. B. Liu, W. X. Feng, X. D. Xu and W. Yao, Coupled spin and valley physics in monolayers of MoS_2 and other group-VI dichalcogenides, *Phys. Rev. Lett.*, 2012, **108**, 196802.

27 Q. H. Wang, K. Kalantar-Zadeh, A. Kis, J. N. Coleman and M. S. Strano, Electronics and optoelectronics of two-dimensional transition metal dichalcogenides, *Nat. Nanotechnol.*, 2012, **7**, 699–712.

28 X. X. Xi, Z. Wang, W. Zhao, J.-H. Park, K. T. Law, H. Berger, L. Forró, J. Shan and K. F. Mak, Ising pairing in superconducting $NbSe_2$ atomic layers, *Nat. Phys.*, 2016, **12**, 139–143.

29 A. Hasani, M. Tekalgne, Q. V. Le, H. W. Jang and S. Y. Kim, Two-dimensional materials as catalysts for solar fuels: hydrogen evolution reaction and CO_2 reduction, *J. Mater. Chem. A*, 2019, **7**, 430−454.

30 W. Feng, W. Pang, Y. Xu, A. Guo, X. Gao, X. Qiu and W. Chen, Transition metal selenides for electrocatalytic hydrogen evolution reaction, *ChemElectroChem*, 2020, **7**, 31−54.

31 B. Ma, X. Li, D. Li and K. Lin, A difunctional photocatalytic H_2 evolution composite Co-catalyst tailored by integration with earth-abundant material and ultralow amount of noble metal, *Appl. Catal. B*, 2019, **256**, 117865.

32 D. W. Wakerley, M. F. Kuehnel, K. L. Orchard, K. H. Ly, T. E. Rosser and E. Reisner, Solar driven reforming of lignocellulose to H_2 with a CdS/CdO_x photocatalyst, *Nat. Energy*, 2017, **2**, 17021.

33 Q. Lia, T. Shi, X. Li, K. Lva, M. Lia, F. Liu, H. Li and M. Lei, Remarkable positive effect of $Cd(OH)_2$ on CdS semiconductor for visible-light photocatalytic H_2 production, *Appl. Catal. B*, 2018, **229**, 8–14.

34 K. Maeda, G. Sahara, M. Eguchi and O. Ishitani, Hybrids of a ruthenium(II) polypyridyl complex and a metal oxide nanosheet for dye-sensitized hydrogen evolution with visible light: effects of the energy structure on photocatalytic

activity, *ACS Catal.*, 2015, **5**, 1700–1707.
35 J. Di, C. Yan, A. D. Handoko, Z. W. Seh, H. Li and Z. Liu, Ultrathin two-dimensional materials for photo- and electrocatalytic hydrogen evolution, *Mater. Today*, 2018, **21**, 749–770.
36 X. Wang, Y. Chen, B. Zheng, F. Qi, J. He, Q. Li, P. Li and W. Zhang, Graphene-like WSe_2 nanosheets for efficient and stable hydrogen evolution, *J. Alloys Compd.*, 2017, **691**, 698−704.
37 H.-H. Wu, H. Huang, J. Zhong, S. Yu, Q. Zhang and X. C. Zeng, Monolayer triphosphates MP_3 (M = Sn, Ge) with excellent basal catalytic activity for hydrogen evolution reaction, *Nanoscale*, 2019, **11**, 12210−12219.
38 Z. W. Seh, K. D. Fredrickson, B. Anasori, J. Kibsgaard, A. L. Strickler, M. R. Lukatskaya, Y. Gogotsi, T. F. Jaramillo and A. Vojvodic, Two-dimensional molybdenum carbide (MXene) as an efficient electrocatalyst for hydrogen evolution, *ACS Energy Lett.*, 2016, **1**, 589−594.
39 B. Zhang, J. Zhou, Z. Guo, Q. Peng and Z. Sun, Two-dimensional chromium boride MBenes with high her catalytic activity, *Appl. Surf. Sci.*, 2020, **500**, 144248.
40 Q. Tang, D. E. Jiang, Mechanism of Hydrogen Evolution Reaction on 1T-MoS2 from First Principles, *ACS Catal.* 2016, 6, 8, 4953–4961.
41 B. Hinnemann, P. G. Moses, J. Bonde, K. P. Jørgensen, J. H. Nielsen and S. Horch, Biomimetic hydrogen evolution: MoS_2 nanoparticles as catalyst for hydrogen evolution, *J. Am. Chem. Soc.*, 2005, **127**, 5308–5309.
42 T. F. Jaramillo, K. P. Jørgensen, J. Bonde, J. H. Nielsen, S. Horch and I. Chorkendorff, Identification of active edge sites for electrochemical H_2 evolution from MoS_2 nanocatalysts, *Science*, 2007, **317**, 100–102.
43 H. Wang, Y. Wu, T. Xiao, X. Yuan, G. Zeng, W. Tu, S. Wu, H. Y. Lee, Y. Z. Tan and J. W. Chew, Formation of quasi-core-shell In_2S_3/anatase TiO_2@metallic $Ti_3C_2T_x$ hybrids with favorable charge transfer channels for excellent visible-light photocatalytic performance, *Appl. Catal. B*, 2018, **233**, 213–225.
44 D. Huang, G. Zhang, J. Yi, M. Cheng, C. Lai, P. Xu, C. Zhang, Y. Liu, C. Zhou and W. Xue, Progress and challenges of metal-organic frameworks-based materials for SR-AOPs applications in water treatment, *Chemosphere*, 2021, **263**, 127672.
45 I. Papailias, N. Todorova, T. Giannakopoulou, N. Ioannidis, P. Dallas, D. Dimotikali and C. Trapalis, Novel torus shaped g-C_3N_4 photocatalysts, *Appl. Catal. B*, 2020, **268**, 118733.
46 C. Karthikeyan, P. Arunachalam, K. Ramachandran, A. M. Al-mayouf and S. Karuppuchamy, Recent advances in semiconductor metal oxides with enhanced methods for solar photocatalytic applications, *J. Alloys Compd.*, 2020, **828**, 154281.
47 A. Fujishima and K. Honda, Electrochemical photolysis of water at a semiconductor electrode, *Nature*, 1972, **238**, 37–38.
48 S. Gu, Y. Chen, X. Yuan, H. Wang, X. Chen, Y. Liu, Q. Jiang, Z. Wu and G. Zeng, Facile synthesis of CeO_2 nanoparticle sensitized CdS nanorod photocatalyst with improved visible-light photocatalytic degradation of rhodamine B, *RSC Adv.*, 2015, **5**, 79556–79564.
49 R. Abinaya, J. Archana, S. Harish, M. Navaneethan, S. Ponnusamy, C. Muthamizhchelvan, M. Shimomura and Y. Hayakawa, Ultrathin layered MoS_2 nanosheets with rich active sites for enhanced visible light photocatalytic activity, *RSC Adv.*, 2018, **8**, 26664–26675.
50 U. Vool, A. Hamo, G. Varnavides, Y. Wang, T. X. Zhou, N. Kumar, Y. Dovzhenko,

Z. Qiu, C.A.C. Garcia, A. T. Pierce, J. Gooth, P. Anikeeva, C. Felser, P. Narang and A. Yacoby, Imaging phonon-mediated hydrodynamic flow in WTe_2, *Nat. Phys.*, 2021, **17**, 1216–1220.

51 S. Haldar, H. Vovusha, M. K. Yadav, O. Eriksson and B. Sanyal, Systematic study of structural, electronic, and optical properties of atomic-scale defects in the two-dimensional transition metal dichalcogenides MX_2 (M = Mo, W, X = S, Se, Te), *Phys. Rev. B*, 2015, **92**, 235408.

52 L. Yu, Q. Yan and A. Ruzsinszky, Negative Poisson's ratio in 1T-type crystalline two-dimensional transition metal dichalcogenides, *Nat. Commun.*, 2017, **8**, 15224.

53 X. Lv, L. Yu, F. Li, J. Gong, Y. He and Z. Chen, Penta-MS_2 (M = Mn, Ni, Cu/Ag and Zn/Cd) monolayers with negative Poisson's ratios and tunable bandgaps as water-splitting photocatalysts, *J. Mater. Chem. A*, 2021, **9**, 6993−7004.

54 J. Gu, Z. Zhao, J. Huang, B. G. Sumpter and Z. Chen, MX anti-MXenes from non-van der Waals bulks for electrochemical applications: the merit of metallicity and active basal plane, *ACS Nano*, 2021, **15**, 6233–6242.

55 X. Qiao, X. Lv, Y. Dong, Y. Yang and F. Li, Two-dimensional V-VI binary nanosheets with square lattice: a theoretical investigation, *Phys. Status Solidi B*, 2021, 2100178.

56 Y. Huang, Y.-H. Pan, R. Yang, L.-H. Bao, L. Meng, H.-L. Luo, Y.-Q. Cai, G.-D. Liu, W.-J. Zhao, Z. Zhou, L.-M. Wu, Z.-L. Zhu, M. Huang, L.-W. Liu, L. Liu, P. Cheng, K.-H. Wu, S.-B. Tian, C.-Z. Gu, Y.-G. Shi, Y.-F. Guo, Z. G. Cheng, J.-P. Hu, L. Zhao, G.-H. Yang, E. Sutter, P. Sutter, Y.-L. Wang, W. Ji, X.-J. Zhou and H.-J. Gao, Universal mechanical exfoliation of large-area 2D crystals, *Nat. Commun.*, 2020, **11**, 2453.

57 G. Kresse and J. Furthmüller, Efficient iterative schemes for *ab initio* total-energy calculations using a plane-wave basis set, *Phys. Rev. B*, 1996, **54**, 11169–11186.

58 G. Kresse and D. Joubert, From ultrasoft pseudopotentials to the projector augmented-wave method, *Phys. Rev. B*, 1999, **59**, 1758–1775.

59 P. E. Blöchl, Projector augmented-wave method, *Phys. Rev. B*, 1994, **50**, 17953–17979.

60 J. P. Perdew, K. Burke and M. Ernzerhof, Generalized gradient approximation made simple, *Phys. Rev. Lett.*, 1996, **77**, 3865–3868.

61 H. J. Monkhorst and J. D. Pack, Special points for Brillouin-zone integrations, *Phys. Rev. B*, 1976, **13**, 5188–5192.

62 J. Heyd, G. E. Scuseria and M. Ernzerhof, Hybrid functionals based on a screened coulomb potential, *J. Phys. Chem. C*, 2003, **118**, 8207–8215.

63 S. Baroni, S. de Gironcoli, A. Dal Corso and P. Giannozzi, Phonons and related crystal properties from density-functional perturbation theory, *Rev. Mod. Phys.*, 2001, **73**, 515–562.

64 L.-M. Yang, V. Bacic, I. A. Popov, A. I. Boldyrev, T. Heine, T. Frauenheim and E. Ganz, Two-dimensional Cu_2Si monolayer with planar hexacoordinate copper and silicon bonding, *J. Am. Chem. Soc.*, 2015, **137**, 2757−2762.

65 F. B. Romdhane, O. Cretu, L. Debbichi, O. Eriksson, S. Lebegue and F. Banhart, Quasi-2D Cu_2S crystals on graphene: in-situ growth and *ab-initio* calculations, *Small*, 2015, **11**, 1253−1257.

66 X. Wang, Y. Gong, G. Shi, W. L. Chow, K. Keyshar, G. Ye, R. Vajtai, J. Lou, Z. Liu and E. Ringe, Chemical vapor deposition growth of crystalline monolayer $MoSe_2$, *ACS Nano*, 2014, **8**, 5125−5131.

67 V. Zólyomi, N. D. Drummond and V. I. Fal'ko, Electrons and phonons in single

layers of hexagonal indium chalcogenides from *ab initio* calculations, *Phys. Rev. B*, 2014, **89**, 205416.
68 M. Sánchez and L. Wirtz, Phonons in single-layer and few-layer MoS_2 and WS_2, *Phys. Rev. B*, 2011, **84**, 155413.
69 G. Qin, Q. B. Yan, Z. Qin, S. Y. Yue, M. Hu and G. Su, Anisotropic intrinsic lattice thermal conductivity of phosphorene from first principles, *Phys. Chem. Chem. Phys.*, 2015, **17**, 4854–4858.
70 J. Wang, S. Yip, S. R. Phillpot and D. Wolf, Crystal instabilities at finite strain, *Phys. Rev. Lett.*, 1993, **71**, 4182–4185.
71 Y. Wang, J. Lv, L. Zhu and Y. Ma, CALYPSO: a method for crystal structure prediction, *Comput. Phys. Commun.*, 2012, **183**, 2063–2070.
72 W. Jin, J. Pang, L. Yue, M. Xie, X. Kuang and C. Lu, Multifunctional PbS_2 monolayer with an in-plane negative Poisson ratio and photocatalytic water splitting properties, *J. Phys. Chem. Lett.*, 2022, **13**, 10494–1049.
73 A. Savin, R. Nesper, S. Wengert and T. F. Fässler, ELF: the electron localization function, *Angew. Chem. Int. Ed.*, 1997, **36**, 1808–1832.
74 V. Wang and W. T. Geng, Lattice defects and the mechanical anisotropy of borophene, *J. Phys. Chem. C*, 2017, **121**, 10224–10232.
75 R. C. Andrew, R. E. Mapasha, A. M. Ukpong and N. Chetty, Mechanical properties of graphene and boronitrene, *Phys. Rev. B*, 2012, **85**, 125428.
76 Q. Peng and S. De, Outstanding mechanical properties of monolayer MoS_2 and its application in elastic energy storage, *Phys. Chem. Chem. Phys.*, 2013, **15**, 19427–19437.
77 I. N. Frantsevich, F. F. Voronov and S. A. Bokuta, Elastic constants and elastic moduli of metals and insulators handbook, *ed I N Frantsevich (Kiev: Naukova Dumka)*, 1983, pp 60–180.
78 R. S. Lakes and K. Elms, Indentability of conventional and negative Poisson's ratio foams, *J. Compos. Mater.*, 1993, **27**, 1193−1202.
79 J. B. Choi and R. S. Lakes, Fracture toughness of re-entrant foam materials with a negative Poisson's ratio: experiment and analysis, *Int. J. Fract.*, 1996, **80**, 73−83.
80 K. E. Evans and A. Alderson, Auxetic materials: functional materials and structures from lateral thinking, *Adv. Mater.*, 2000, **12**, 617−628.
81 J. Jiang and H. Park, Negative Poisson's ratio in single-layer black phosphorus, *Nat. Commun.*, 2014, **5**, 4727.
82 H. Zhong, K. Huang, G. Yu and S. Yuan, Electronic and mechanical properties of few-layer borophene, *Phys. Rev. B*, 2018, **98**, 054104.
83 X. Lv, L. Yu, F. Li, J. Gong, Y. He and Z. Chen, Penta-MS_2 (M = Mn, Ni, Cu/Ag and Zn/Cd) monolayers with negative Poisson's ratios and tunable bandgaps as water-splitting photocatalysts, *J. Mater. Chem. A*, 2021, **9**, 6993−7004.
84 X. Chen, D. Wang, X. Liu, L. Li and B. Sanyal, Two-dimensional square-A_2B (A = Cu, Ag, Au, and B = S, Se): auxetic semiconductors with high carrier mobilities and unusually low lattice thermal conductivities, *J. Phys. Chem. Lett.*, 2020, **11**, 2925−2933.
85 J. He, G. Ding, C. Zhong, S. Li, D. Li and G. Zhang, Cr_2TiC_2-based double MXenes: novel 2D bipolar antiferromagnetic semiconductor with gate-controllable spin orientation toward antiferromagnetic spintronics, *Nanoscale*, 2019, **11**, 356−364.
86 M. An, Y. Zhang, J. Chen, H.-M. Zhang, Y. Guo and S. Dong, Tuning magnetism in layered magnet VI_3: a theoretical study, *J. Phys. Chem. C*, 2019, **123**, 30545−30550.

87 G. Wang, Theoretical prediction of the intrinsic half-metallicity in surface-oxygen-passivated Cr_2N MXene, *J. Phys. Chem. C*, 2016, **120**, 18850−18857.
88 S.-S. Li, S.-J. Hu, W.-X. Ji, P. Li, K. Zhang, C.-W. Zhang and S.-S. Yan, Emergence of ferrimagnetic half-metallicity in two-dimensional MXene $Mo_3N_2F_2$, *Appl. Phys. Lett.*, 2017, **111**, 202405.
89 J. He, P. Lyu and P. Nachtigall, New two-dimensional Mn-based MXenes with room-temperature ferromagnetism and half-metallicity, *J. Mater. Chem. C*, 2016, **4**, 11143−11149.
90 J.-A. Yan and L. Webster, Strain-tunable magnetic anisotropy in monolayer $CrCl_3$, $CrBr_3$, and CrI_3, *Phys. Rev. B*, 2018, **98**, 144411.
91 B. Huang, G. Clark, E. Navarro-Moratalla, D. R. Klein, R. Cheng, K. L. Seyler, D. Zhong, E. Schmidgall, M. A. McGuire and D. H. Cobden, Layer-dependent ferromag-netism in a van der Waals crystal down to the monolayer limit, *Nature*, 2017, **546**, 270.
92 C. Zhang, Y. Nie, S. Sanvito and A. Du, First-principles prediction of a room-temperature ferromagnetic janus VSSe monolayer with piezoelectricity, ferroelasticity, and large valley polarization, *Nano Lett.*, 2019, **19**, 1366–1370.
93 L. Webster and J.-A. Yan, Strain-tunable magnetic anisotropy in monolayer $CrCl_3$, $CrBr_3$, and CrI_3, *Phys. Rev. B*, 2018, **98**, 144411.
94 W.-B. Zhang, Q. Qu, P. Zhu and C.-H. Lam, Robust intrinsic ferromagnetism and half semiconductivity in stable two-dimensional single-layer chromium trihalides, *J. Mater. Chem. C*, 2015, **3**, 12457−12468.
95 X. Li and J. Yang, First-principles design of spintronics materials, *Nat. Sci. Rev.*, 2016, **3**, 365–381.
96 H. Moulkhalwa, Y. Zaoui and K. O. Obodo, Half-metallic and half-semiconductor gaps in Cr-based chalcogenides: DFT + U calculations, *J. Supercond. Nov. Magn.*, 2019, **32**, 635–649.
97 X. Wang, J. Tan, C. Han, J.-J. Wang, L. Lu, H. Du, C.-L. Jia, V. L. Deringer, J. Zhou and W. Zhang, Sub-angstrom characterization of the structural origin for high in-plane anisotropy in 2D GeS_2, *ACS Nano*, 2020, **14**, 4456−4462.
98 V. K. Sangwa and M. C. Hersam, Electronic transport in two-dimensional materials, *Annu. Rev. Phys. Chem.*, 2018, **69**, 299−325.
99 J. Bardeen and W. Shockley, Deformation potentials and mobilities in non-polar crystals, *Phys. Rev.*, 1950, **80**, 72−80.
100 J. Qiao, X. Kong, Z.-X. Hu, F. Yang and W. Ji, High-mobility transport anisotropy and linear dichroism in few-layer black phosphorus, *Nat. Commun.*, 2014, **5**, 4475.
101 H. V. Phuc, N. N. Hieu, B. D. Hoi, N. V. Hieu, T. V. Thu, N. M. Hung, V. V. Ilyasov, N. A. Poklonski and C. V. Nguyen, Tuning the electronic properties, effective mass and carrier mobility of MoS_2 monolayer by strain engineering: first-principles calculations, *J. Electron. Mater.*, 2018, **47**, 730–736.
102 L. Xu, P. Zhang, H. Jiang, X. Wang, F. Chen, Z. Hu, Y. Gong, L. Shang, J. Zhang, K. Jiang and J. Chu, Large-scale growth and field-effect transistors electrical engineering of atomic-layer SnS_2, *Small*, 2019, **15**, 1904116.
103 Y. Li, Y. L. Li, C. M. Araujo, W. Luo and R. Ahuja, Single-layer MoS_2 as an efficient photocatalyst, *Catal. Sci. Technol.*, 2013, **3**, 2214–2220.
104 S. Saha and T.P. Sinha, Electronic structure, chemical bonding, and optical properties of paraelectric $BaTiO_3$, *Phys. Rev. B*, 2000, **62**, 8828–8834.
105 J. Y. Gan, F. H. Li, Y. R. Tang and Q. Tang, Theoretical study of transition-metal-modified Mo_2CO_2 MXene as a catalyst for the hydrogen evolution reaction,

ChemSusChem, 2020, **13**, 6005−6015.
106 J. K. Nørskov, T. Bligaard, A. Logadottir, J. R. Kitchin, J. G. Chen, S. Pandelov and U. Stimming, Trends in the exchange current for hydrogen evolution, *J. Electrochem. Soc.*, 2005, **152**, J23−J26.
107 J. Zhou, J. Lin, X. Huang, Y. Zhou, J. Xia, H. Wang, Y. Xie, H. Yu, J. Lei, D. Wu, G. Liu and Z. Liu, A library of atomically thin metal chalcogenides, *Nature*, 2018, **556**, 355–359.
108 J. Zhou, C. Zhu, Y. Zhou, J. Dong, P. Li, Z. Zhang, Z. Wang, Y.-C. Lin, J. Shi, R. Zhang, Y. Zheng, H. Yu, B. Tang, F. Liu, L. Wang, L. Liu, G.-B. Liu, W. Hu, Y. Gao, H. Yang, W. Gao, L. Lu, Y. Wang, K. Suenaga, G. Liu, F. Ding, Y. Yao and Z. Liu, Composition and phase engineering of metal chalcogenides and phosphorous chalcogenides, *Nat. Mater.*, **2023**, *22*, 450–458.